

Anisotropic Approach for Simulating Electron Transport in Layered Materials: Computational and Experimental Study of Highly Oriented Pyrolytic Graphite

Martina Azzolini,^{*,†,‡} Tommaso Morresi,^{†,‡} Kerry Abrams,[¶] Robert Masters,[¶] Nicola Stehling,[¶] Cornelia Rodenburg,[¶] Nicola M. Pugno,^{‡,§,||} Simone Taioli,^{†,⊥} and Maurizio Dapor^{*,†,||}

[†]European Centre for Theoretical Studies in Nuclear Physics and Related Areas (ECT*-FBK) and Trento Institute for Fundamental Physics and Applications (TIFPA-INFN), Trento, Italy

[‡]Laboratory of Bio-Inspired and Graphene Nanomechanics, Department of Civil, Environmental and Mechanical Engineering, University of Trento, Trento, Italy

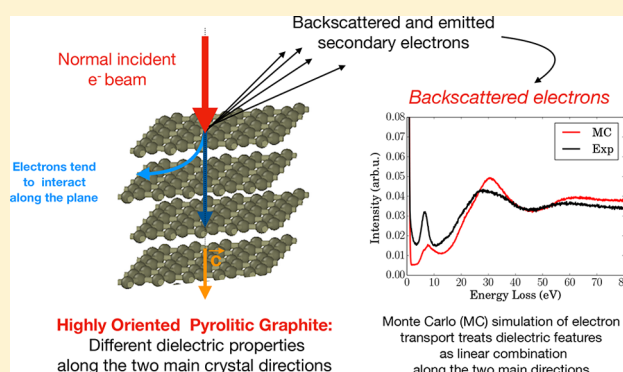
[¶]Department of Materials Science and Engineering, University of Sheffield, Sheffield, United Kingdom

[§]Ket-Lab, Edoardo Amaldi Foundation, Italian Space Agency, Rome, Italy

^{||}School of Engineering and Materials Science, Queen Mary University of London, London, United Kingdom

[⊥]Faculty of Mathematics and Physics, Charles University, Prague, Czech Republic

ABSTRACT: In this work, we propose a theoretical and computational model for taking into account the anisotropic structure of highly oriented pyrolytic graphite (HOPG) in the Monte Carlo simulations of charge transport. In particular, the dielectric characteristics, such as the inelastic mean free path and energy losses, are treated by linearly combining the contributions to these observables along the two main orthogonal directions identifying the layered crystalline structure of HOPG (along the layer plane and perpendicular to it). Energy losses are evaluated from ab initio calculations of the dielectric function of the system along these two perpendicular directions. Monte Carlo simulated spectra, obtained with our anisotropic approach, are compared with acquired experimental data of reflection electron energy loss and secondary electron spectra, showing a good agreement. These findings validate the idea of the importance of considering properly weighted interplanar and intraplanar interactions in the simulation of electron transport in layered materials.



INTRODUCTION

Carbon-based materials have recently attracted significant attention due to the discovery of new exciting science, particularly in connection with the unique band structure of graphene. Within this 2D material, in which the planar topology is realized by a sp^2 -net of carbon atoms, electrons behave like relativistic Fermions offering the potential for high-speed nanoscale electronics and for replacing silicon in lightweight and wearable devices. Other carbon allotropes, obtained for example by rolling up graphene in carbon nanotubes, display further interesting properties, as they can be produced with both semiconducting and metallic character depending on the twist and on the diameter of the tube.^{1,2} Nevertheless, these materials are still difficult to be synthesized in a cost-effective, scalable way.

At variance with other allotropes of carbon, graphite can be naturally found (the others two being amorphous carbon and diamond). Thus, it is worthy to explore its properties, particularly with respect to its electronic characteristics for

applications in optoelectronic devices and imaging. Graphite represents a 3D stacking of graphene sheets and thus displays an uniaxial layered structure which retains some characteristics of graphene, while its thermal, acoustic, and electronic properties are highly anisotropic. Most notably, the large anisotropy of the electric conductivity means that along the planes graphite shows a higher conductivity than in the direction normal to the surface.³

In this work we present Monte Carlo (MC) simulations of reflection electron energy loss (REEL) and secondary electron (SE) spectra of highly oriented pyrolytic graphite (HOPG), taking into account the target anisotropic structure. Simulated spectra are compared with experimental data recorded in our laboratories. In this model, elastic scattering events between electrons and target atoms are treated via the Mott theory,⁴

Received: March 7, 2018

Revised: April 13, 2018

Published: April 16, 2018

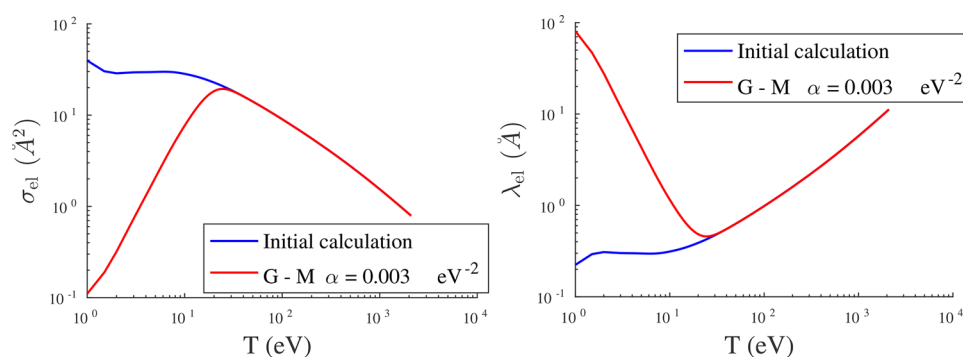


Figure 1. Total elastic scattering cross section σ_{el} (left panel) and elastic mean free path λ_{el} (right panel) calculated from the bare Mott theory (blue line) and by using the correction proposed by Ganachaud and Mokrani ($\alpha = 0.003 \text{ 1/eV}^2$) (red line).

which is based on the solution of the Dirac equation in a central field. At variance, inelastic collisions between the primary electron beam and the electron cloud of the target can result in the excitation of bulk and surface plasmon oscillations. In this regard, an accurate description of the electron energy loss is provided by the dielectric theory developed by Ritchie.³ Within this approach, the key quantity for the calculation of the inelastic cross section is the energy loss function (ELF), defined as the imaginary part of the inverse of the dielectric function $\epsilon(\vec{q}, W)$, where \vec{q} is the transferred momentum owing to the inelastic interactions and W is the energy loss.

To take into account graphite anisotropy, we assess from ab initio time-dependent density functional simulations the dielectric function optical limit ($\epsilon_{\vec{q} \rightarrow 0}$) along two orthogonal directions: along the direction normal to the layer (identified by the vector \vec{z}), which accounts for interplanar interactions, and along the one perpendicular to \vec{z} , which describes intraplanar excitations (in-plane direction). Finally, the ELFs, obtained by combining these two dielectric functions, were fitted in the optical limit by using Drude–Lorentz functions and extended to finite momenta by a dispersion law obtained within the random phase approximation (RPA).⁶ In this way, the energy losses in both planar and interplanar directions were taken into account appropriately in our Monte Carlo simulations.

In the following sections the Monte Carlo model as well as the experimental procedures will be described in detail. Then the comparison between experimental and simulated spectra will be presented.

■ EXPERIMENTAL DETAILS

Reflection Electron Energy Loss Spectra Acquisition.

The sample of HOPG was initially cleaved ex situ and then was cleaned by annealing at 600 °C for 10 min in ultrahigh vacuum. The REEL measurements were realized at a base pressure of $\approx 2 \times 10^{-2}$ mbar in a PHI 545 system. The experimental apparatus is composed by a coaxial electron gun, a nonmonochromatic MgK α ($h\nu = 1253.6 \text{ eV}$) X-ray source, a He discharge lamp, and double-pass cylindrical mirror analyzer (CMA). In CMA, the angle between primary electron beam and the surface normal is maintained constant, while emitted electrons cross the surface in different directions that are described by the angle between the surface normal and the CMA axis (30°), the entrance angle to the analyzer ($42^\circ \pm 6^\circ$), and the azimuth angle in a plane normal to the CMA axis. The energy resolution was maintained constant at 0.6 eV, as measured on a Pd Fermi edge. The zero-loss peak has a measured full width at half-maximum of 0.9 eV. The energy of the impinging electron

beam spans the range from 250 to 2000 eV. The acquired spectra are corrected for the energy dependence ($E^{-0.9}$) according to the analyzer transmission function.

Secondary Electron Spectrum Acquisition.

SE spectrum acquisition was performed with a FEI Helios NanoLab G3 UC scanning electron microscope (SEM). HOPG with a mosaic spread of $3.55^\circ \pm 1.5^\circ$ (purchased from Agar scientific) was mounted on an aluminum pin-stub using silver paint. Prior to specimen insertion into the SEM, the HOPG surface was mechanically exfoliated. The maximum time between exfoliation, insertion into the SEM vacuum chamber, and pump down to vacuum was less than 3 min. For imaging and spectra collection, the vacuum pressure at room temperature was 3×10^{-6} mbar, and the working distance was kept to 4 mm. The design of the in-lens detector of this SEM allows the collection of different SE energy ranges by changing a mirror electrode voltage (M parameter). Images were collected at different M settings ranging from minimum electron energy of -0.7 eV to a maximum of 12.7 eV. SE spectra were collated by differentiating the mean intensity of each image from each individual M step. The SE energy calibration method for this system can be found in Young et al.⁷ and the Supporting Information of Wan et al.,⁸ while the absolute energy value was checked by fine structures reported experimentally in literature (3, 4, and 7.5 eV⁹) for HOPG and fine structure for diamond (6 eV¹⁰). Detection artifacts within a certain M range were identified by evaluating the average intensity of a reference gold sample with the smallest possible filter parameter step difference (0.1 V). The artifacts manifested as an increment in M without an associated signal change, signifying a discrepancy between the stated and actual M . A lookup table of corrected M was created, excluding the artifacts and rescaling the remaining M to the initial filter parameter collection range. The differentiation of the S-curve to obtain the spectrum was performed using the corrected SE energy values associated with the respective M values.

■ COMPUTATIONAL DETAILS

Elastic Scattering. Elastic scattering between the impinging electrons and the atoms of the target is described by the Mott theory (see, for example, refs 11–15). The atomic potential was obtained self-consistently by solving the Dirac–Kohn–Sham equations for the carbon atom within the local spin-density approximation (LSDA) as implemented in the ELK software program.¹⁶ The elastic scattering cross section is calculated as reported in ref 17.

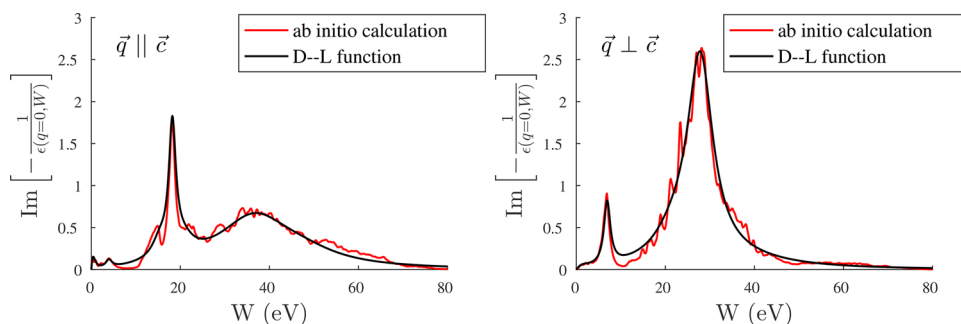


Figure 2. ELF functions along the two possible orthogonal directions of transferred momentum \vec{q} : ab initio calculations (red lines) are compared to the Drude–Lorentz best fits (black lines).

For $T = 10$ eV we find a total elastic scattering cross section $\sigma_{el} = 28.3 \text{ \AA}^2$ and an elastic mean free path $\lambda_{el} = 0.31 \text{ \AA}$. This value of λ_{el} is 1 order of magnitude lower than the lattice parameters of graphite ($\vec{a} = 2.46 \text{ \AA}$, $\vec{c} = 6.71 \text{ \AA}$) and is thus unphysical. Therefore, we introduce a correction to the Mott cross section at low energy.¹⁸ Ganachaud and Mokrani¹⁹ proposed to multiply the total elastic scattering cross section σ_{el} by a cutoff function in order to diminish σ_{el} at low energy. Similarly to this model, the total elastic scattering cross section can be obtained by multiplying the cross section calculated using the partial-wave expansion method by the following factor

$$R(T) = \tanh(\alpha T^2) \quad (1)$$

where α is a parameter to be determined. It is worth noting that in the previous function, the α parameter is different from the α_C parameter of the Ganachaud and Mokrani cutoff function. Indeed, the latter includes also the material energy band gap. By choosing $\alpha = 0.003 \text{ eV}^{-2}$, the value of the elastic mean free path for $T = 10$ eV is $\lambda_{el} = 1.15 \text{ \AA}$. Figure 1 shows the behavior of σ_{el} (left panel) and λ_{el} (right panel) obtained with $\alpha = 0.003 \text{ eV}^{-2}$, along with those calculated by using the bare Mott theory. By introducing this factor, one obtains a behavior of the elastic scattering cross section consistently decreasing at low energy.

Moreover, we find out that the use of a cutoff function is necessary to obtain good agreement between calculated and experimental SE spectra.

Inelastic Scattering. The inelastic scattering between the impinging electrons and the electron clouds of the target atoms was dealt with using the Ritchie theory.⁵

Within this approach, the total inelastic cross section can be computed by assessing the inelastic mean free path λ_{inel} (IMFP). The latter can be obtained by integrating over the energy loss interval the differential inverse inelastic mean free path (DIIMFP)

$$\lambda_{inel}^{-1} = \int_0^{T/2} \frac{d\lambda_{inel}^{-1}}{dW} dW \quad (2)$$

where T is the primary beam kinetic energy and the DIIMFP is defined as

$$\frac{d\lambda_{inel}^{-1}}{dW} = \frac{1}{\pi T a_0} \int_{q_-}^{q_+} \frac{dq}{q} \text{Im} \left[-\frac{1}{\epsilon(\vec{q}, W)} \right] \quad (3)$$

where a_0 is the Bohr radius. The limits of integration of the integral in eq 3 are set to $q_{\pm} = \sqrt{2mT} \pm \sqrt{2m(T - W)}$ for momentum conservation.¹¹ The integrand in eq 3 is the so-called ELF.

According to eq 3, to model the inelastic collisions one needs to compute the dielectric function of the target material as a function of the momentum \vec{q} and of the energy transferred during the inelastic collision W . ELFs were calculated in the optical limit ($\vec{q} \rightarrow 0$) from ab initio simulations using the ELK code¹⁶ within the framework of linear response time-dependent density functional theory (LR-TDDFT). In these calculations we used a k -point sampling of $20 \times 20 \times 20$ mesh points, a cutoff for augmented plane waves equal to 400 eV, and a Fermi-smearing of 0.2 eV.

Considering the anisotropic structure of HOPG, two possible different orientations for energy losses were taken into account: on the one hand, we considered the transferred momentum \vec{q} parallel to the vector normal to the graphite plane (identified by the vector \vec{c}) and on the other hand \vec{q} perpendicular to \vec{c} . Dielectric functions and derived observables, such as inelastic mean free paths, are reported for these two cases in the following discussion respectively as $\epsilon_{\parallel}(q, W)$ and $\epsilon_{\perp}(q, W)$, and the same notation is applied to the inelastic mean free paths λ_{\parallel} and λ_{\perp} . Optical ELFs were then fitted by Drude–Lorentz (D–L) functions as follows

$$\text{ELF} = \sum_n \frac{A_n \Gamma_n W}{(E_n^2(q) - W^2)^2 - (\Gamma_n W)^2} \quad (4)$$

where A_n is the excitation strength of the n th oscillator, Γ_n the damping constant, and E_n the plasmon excitation energy. In Figure 2 ab initio data and final fit functions are shown, while in Tables 1 and 2 the fitting parameters are reported. In the fitting

Table 1. D–L Parameters ($\vec{q} \parallel \vec{c}$ Direction)

n	A_n (eV ²)	Γ_n (eV)	E_n (eV)
1	0.15	1.75	0.80
2	0.62	1.76	4.06
3	13.26	4.22	15.57
4	51.80	1.90	18.23
5	25.52	6.23	20.73
6	452.31	20.02	37.93
7	112.91	19.84	48.25

procedure the number of oscillators was chosen to reproduce the ab initio spectra. Moreover, the choice of these optimal parameters leads to fulfilling the f -sum rule.

Finally, ELF fit functions are extended to finite values of \vec{q} by applying the quadratic dispersion law obtained within the RPA.⁶

Table 2. D–L Parameters ($\vec{q} \perp \vec{c}$ Direction)

n	A_n (eV ²)	Γ_n (eV)	E_n (eV)
1	0.43	5.36	2.58
2	8.96	1.73	6.99
3	0.25	8.30	14.53
4	33.93	10.16	21.77
5	32.00	10.50	24.32
6	466.69	6.99	28.03
7	100.30	30.03	38.09

$$E_n(q \neq 0) = E_n(q = 0) + \frac{\hbar^2 q^2}{2m} \quad (5)$$

These data were used to compute the total inelastic scattering cross section σ_{inel} and the IMFP λ_{inel} by eq 2 (see Figure 3).

To calculate the total IMFP by taking into account the anisotropic structure of graphite, λ_{inel} and W were determined by linearly combining at each inelastic interaction the corresponding values along the two possible orthogonal directions of the transferred momentum \vec{q} , as follows

$$\lambda_{\text{inel}} = [f \cos^2 \theta] \lambda_{\parallel} + [(1 - f) + f \sin^2 \theta] \lambda_{\perp} \quad (6)$$

$$W = [f \cos^2 \theta] W_{\parallel} + [(1 - f) + f \sin^2 \theta] W_{\perp} \quad (7)$$

where f is an *anisotropy parameter* in the range [0:1], and θ is the angle between \vec{c} and \vec{q} . The f parameter has been introduced in this anisotropic model of the inelastic observables to favor the electron motion in the planar direction, since HOPG shows a higher conductivity along the plane ($\vec{q} \perp \vec{c}$). The value of f is determined to obtain the best agreement between theoretical and experimental spectra.

Monte Carlo Model. Monte Carlo simulations were performed in order to interpret REEL and SE spectra of HOPG acquired in house. Details on our Monte Carlo approach can be found in ref 21.

To carry out Monte Carlo calculations, some input information about the target material, such as atomic and mass number, density, elastic and inelastic mean free paths, and probability distributions of elastic and inelastic scattering, is required. In particular, the characteristic quantities of the target material are the atomic number ($Z = 6$), the atomic mass ($A = 12.011$ uma),²² the density ($d = 2.25$ g/cm³),²³ the electronic band gap E_g (0.0 eV), and the work function (WF = 4.6 eV).²⁴

On the one hand, in the case of inelastic collisions the primary electrons lose their kinetic energy according to the cumulative probability distribution

$$P_{\text{inel}}(T, W) = \lambda_{\text{inel}} \int_{E_g}^W \frac{d\lambda_{\text{inel}}^{-1}}{dW'} dW' \quad (8)$$

that depends on the initial kinetic energy T and on the energy loss W .

On the other hand, the change in the direction of the elastically scattered electrons can be obtained by using the elastic cumulative probability

$$P_{\text{el}}(T, \bar{\theta}) = \frac{2\pi}{\sigma_{\text{el}}} \int_0^{\bar{\theta}} \frac{d\sigma_{\text{el}}}{d\theta'} \sin \theta' d\theta' \quad (9)$$

that is determined for a fixed initial kinetic energy T by varying the scattering angle θ in the range $[0, \bar{\theta}]$. In eq 9 σ_{el} is the total elastic scattering cross section.

Elastic and inelastic scattering probability distributions lead respectively to the assessment of the scattering angle and of the energy loss. Probability distributions were calculated at specific energies of the electrons, and in Table 3 we report both the electron kinetic energy ranges and the relevant mesh intervals (ΔE) that we used in our MC simulations.

Table 3. Energy Values at Which Scattering Probabilities Are Calculated

range	ΔE (eV)
$0 < E \leq 10$ eV	0.5
$10 < E \leq 50$ eV	1.0
$50 < E \leq 100$ eV	5.0
$100 < E \leq 200$ eV	10.0
$E \geq 200$ eV	100.0

Depending on the kinetic energy of the electron undergoing the collision, we select a probability distribution. The scattering angle (elastic interaction) or the energy loss (inelastic interaction) is determined by generating a random number, uniformly distributed in the interval $[0, 1]$. In fact, (see eq 9) the value of the elastic scattering cumulative probability (or of the inelastic scattering cumulative probability, see eq 8) that equalizes this random number determines the scattering angle (or the energy loss). The total mean free path (λ), which characterizes the electron path within the target material, is defined as

$$\frac{1}{\lambda} = \frac{1}{\lambda_{\text{el}}} + \frac{1}{\lambda_{\text{inel}}} \quad (10)$$

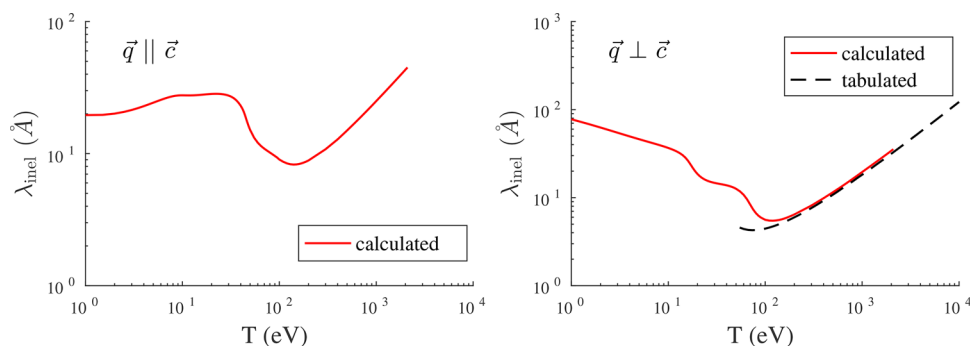


Figure 3. Inelastic mean free paths calculated along the two possible orthogonal directions of transferred momentum \vec{q} . In the case $\vec{q} \perp \vec{c}$, the calculated values are compared with the data by Tanuma et al. (dashed lines).²⁰

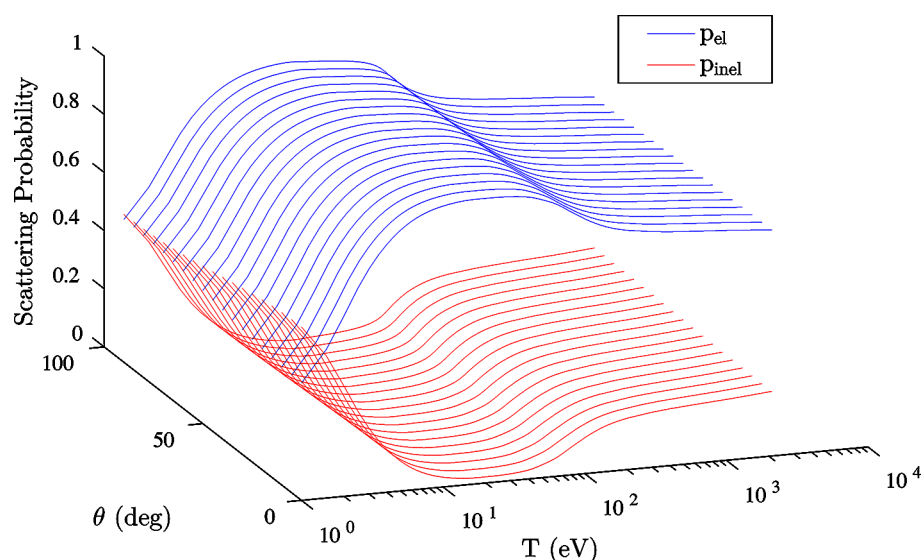


Figure 4. Collision probabilities as a function of the electron kinetic energy (T) and of the angle (θ) between the transferred momentum \vec{q} and the vector \vec{c} normal to the surface.

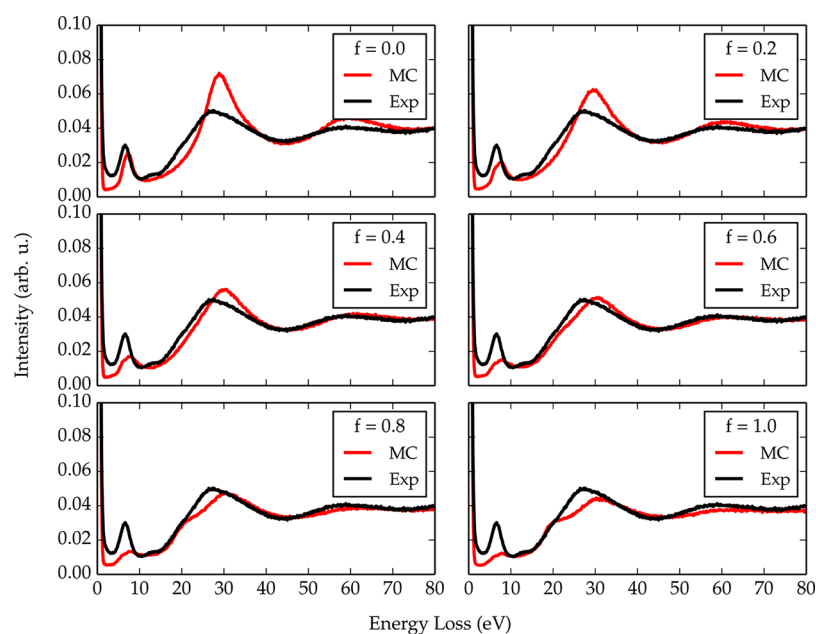


Figure 5. REELS of HOPG for different values of the f parameter (red lines). The kinetic energy of the primary beam is set to 1500 eV. MC calculations are compared with our experimental data (black lines).²¹ The spectra are normalized at a common area of the elastic peak.

where λ_{el} is the elastic mean free path. The probabilities of the elastic and inelastic events can be evaluated, for any fixed value of kinetic energy and angle, as

$$p_{\text{el}} = \frac{\lambda}{\lambda_{\text{el}}} \quad p_{\text{inel}} = \frac{\lambda}{\lambda_{\text{inel}}} \quad (11)$$

The decision on the type of collision that the electrons undergo is made by generating another random number uniformly distributed in the interval $[0, 1]$. When this number is lower than p_{el} the interaction will be elastic; otherwise, it will be inelastic. In Figure 4 we report the elastic and inelastic collision probabilities as a function of the relevant variables θ and T .

RESULTS AND DISCUSSION

REELS. Different simulations were carried out at several beam kinetic energies to simulate our recorded REEL spectra. In the Monte Carlo runs, the trajectories of $N = 10^9$ primary electrons were followed in order to achieve good statistics. The beam incidence angle was fixed at 30° with respect to the normal to the surface, according to our experimental conditions. First, we investigated the dependence of the REEL spectra on the parameter f by spanning a range of possible values in eqs 6 and 7. Figure 5 compares the REEL theoretical spectra (red lines), obtained for an initial kinetic energy of 1500 eV, at different values of f with our experimental data (black lines).²¹

The higher the value of f , the larger the contribution of intraplanar excitations ($\vec{q} \parallel \vec{c}$) to inelastic interactions. This effect

can be noticed in the spectra of Figure 5 by the rise of a shoulder at an energy loss of 20 eV, which corresponds to an oscillation in the ELF along the $\vec{q}||\vec{c}$ direction. The value of the anisotropy parameter that shows the best agreement between experimental and calculated REELS normalized at a common area of the elastic peak is $f = 0.6$. Indeed, by performing a chi-squared test in the energy loss range $[-2:80]$ eV, the lowest value of the χ^2 can be obtained using $f = 0.6$ (see Table 4).

Table 4. χ^2 -Test Carried Out by Considering the Experimental and Calculated Data Normalized at a Common Area of the Elastic Peak in the Energy Loss Range $[-2:80]$ eV for Different Values of the Parameter f

f	χ^2
0.0	134
0.2	207
0.4	125
0.6	93
0.8	95
1.0	174

Nevertheless, a value equal to 0.6 of this anisotropic parameter delivers the best agreement also in other primary beam energy ranges. Thus, we set the anisotropy parameter to this value in all MC simulations. This means physically that by considering, e.g., a scattering angle $\theta = 0^\circ$ (that is, orthogonal to the graphite layers), the energy loss embeds 60% of collisions with a transferred momentum along the $\vec{q}||\vec{c}$ direction, while 40% of the spectrum is made by collisions along the $\vec{q}\perp\vec{c}$ (in-plane) direction (see eqs 6 and 7). Of course, the directional change of the electrons inelastically scattered by the target nuclei is taken into account, for fixed f , by the scattering angle θ , which is modified by the interactions at each MC step. This anisotropic model is consistent with the higher tendency of the electrons to move along the graphite planes rather than across the planes.

MC simulations were performed at several primary beam kinetic energies and compared with our experimental data (normalized at a common area of the elastic peak) in Figure 6.

We notice that the agreement between calculated and experimental data is rather good and becomes progressively better for increasing kinetic energies. This is due to the fact that our experimental spectra report also the contribution of surface plasmons, which is neglected in the MC calculations and whose relative importance diminishes with respect to bulk plasmons at higher values of the primary beam kinetic energy. It is worth noting that the normalization of the data at a common area of the elastic peak keeps the correct intensity ratios between the two main plasmon peaks.

Secondary Electron Spectrum. A quantitative understanding of SE spectra is crucial in imaging techniques. SE emission from graphite was thus assessed by MC simulations, using a kinetic energy of the incident beam ($N = 10^6$) equal to 1000 eV. In the MC simulations, the beam incident direction was chosen orthogonal to the sample surface, according to our experimental conditions (see Experimental Details section). In Figure 7, we compare our MC calculations with the acquired experimental spectra. While the shape of the theoretical and experimental SE spectra is comparable, the simulated spectrum has been shifted by 0.7 eV along the positive axis direction, in order to align the dominant emission peak.

CONCLUSIONS

In this work, we performed Monte Carlo simulations, based on ab initio input data of the energy-dependent dielectric function, of REEL and SE spectra of graphite, taking into account features related to the anisotropic structure of the target material. Graphite has indeed a layered structure, and this must be considered in the treatment of the electron transport properties. In particular, the determination of the inelastic mean free path and of the energy loss was carried out by considering a linear combination of the dielectric properties

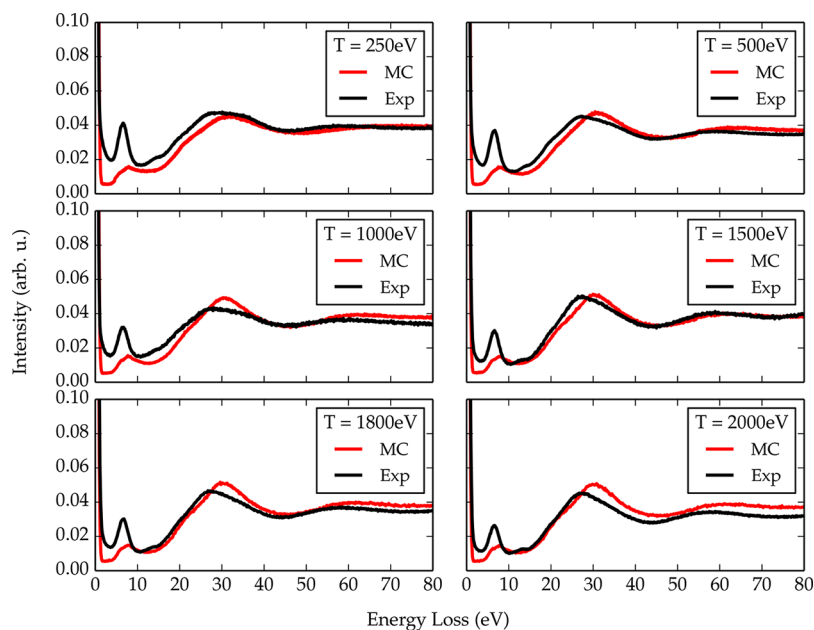


Figure 6. REELS of HOPG for several primary beam kinetic energies. Red lines show simulated spectra, while black curves report our experimental data.²¹ The results are normalized at a common area of the elastic peak.

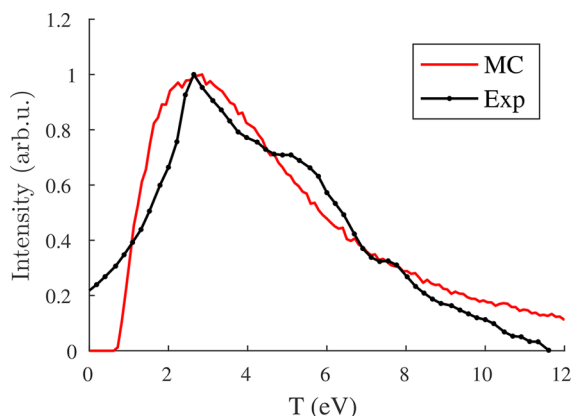


Figure 7. Secondary electron spectra of HOPG. Black line represents experimental data, while in red we report the theoretical spectrum. The data are normalized to a common height of the secondary electron emission peak.

along the two main orthogonal crystal directions (in plane and out of plane).

In our model, the coefficients of these linear combinations depend on an anisotropy parameter f and on the angle between the transferred momentum \vec{q} and the surface normal vector \vec{c} . Our approach for including a dependence of the dielectric properties on the target anisotropy clearly improves the agreement between simulated and experimental REEL spectra. Indeed, spectral features are well reproduced by MC calculations for a value of the anisotropy parameter $f = 0.6$. This means that the energy loss along the $\vec{q} \parallel \vec{c}$ (interplanar) direction contributes to 60% of inelastic collisions, while 40% of the spectral features are contributed by collisions along the $\vec{q} \perp \vec{c}$ direction (in-plane). Furthermore, the MC simulations of secondary emission spectra, whose quantitative understanding is important in imaging applications, were carried out by using our anisotropic model and compared to in-house recorded experimental spectra. We found a good agreement between theoretical and acquired spectra with respect to the line shape, that is, the intensity of the spectral features, while an energy shift was imposed to the theoretical data to reproduce the energy of the main emission peak. These findings demonstrate the importance of considering properly weighted interplanar and intraplanar interactions in the simulation of charge transport in layered materials. Finally, the accuracy of our approach can be tested and possibly improved by considering other descriptions of the ELF at low energies, such as using the Mermin dielectric function presented by Garcia-Molina et al. in ref 25. Moreover, the performance of these models in the optical limit can be further improved by taking into account more rigorously the exchange-correlation effects, particularly at low energy, according to Emfietzoglou et al.^{26,27}

AUTHOR INFORMATION

Corresponding Authors

*E-mail: mazzolini@ectstar.eu.

*E-mail: dapor@ectstar.eu.

ORCID

Nicola M. Pugno: 0000-0003-2136-2396

Simone Taioli: 0000-0003-4010-8000

Maurizio Dapor: 0000-0001-6855-0189

Notes

The authors declare no competing financial interest.

ACKNOWLEDGMENTS

N.M.P. is supported by the European Commission H2020 under the Graphene Flagship Core 2 No. 785219 (WP14 "Polymer Composites") and under the FET Proactive "Neurofibers" No. 732344. C.R. was funded by EPSRC (EP/N008065/1). Access to computing and storage facilities owned by parties and projects contributing to the National Grid Infrastructure MetaCentrum provided under the program "Projects of Large Research, Development, and Innovations Infrastructures" (CESNET LM2015042) is greatly appreciated (<https://www.metacentrum.cz/en/>). The authors gratefully acknowledge the Gauss Centre for Supercomputing for funding this project by providing computing time on the GCS Supercomputer JUQUEEN at Jülich Supercomputing Centre (JSC).²⁸ Furthermore, the authors acknowledge FBK for providing unlimited access to the KORE computing facility.

REFERENCES

- (1) Taioli, S.; Umari, P.; De Souza, M. M. Electronic properties of extended graphene nanomaterials from GW calculations. *Phys. Status Solidi B* **2009**, *246*, 2572–2576.
- (2) Umari, P.; Petrenko, O.; Taioli, S.; De Souza, M. M. Communication: Electronic band gaps of semiconducting zig-zag carbon nanotubes from many-body perturbation theory calculations. *J. Chem. Phys.* **2012**, *136*, 181101.
- (3) Krishnan, K. S.; Ganguli, N. Large anisotropy of the electrical conductivity of graphite. *Nature* **1939**, *144*, 667.
- (4) Mott, N. The scattering of fast electrons by atomic nuclei. *Proc. R. Soc. London, Ser. A* **1929**, *124*, 425.
- (5) Ritchie, R. H. Plasma losses by fast electrons in thin films. *Phys. Rev.* **1957**, *106*, 874.
- (6) Nikjoo, H.; Emfietzoglou, D.; Liamsuwan, T.; Taleei, R.; Liljequist, D.; Uehara, S. Radiation track, DNA damage and response: a review. *Rep. Prog. Phys.* **2016**, *79*, 116601.
- (7) Young, R.; Bosch, E.; Uncovsky, M.; Tuma, L. Low-energy secondary electron filtering with immersion lens SEM. *Microsc. Microanal.* **2009**, *15*, 222.
- (8) Wan, Q.; Abrams, K.; Masters, R.; Talari, A.; Rehman, I.; Claeysens, F.; Holland, C.; Rodenburg, C. Mapping nanostructural variations in silk by secondary electron hyperspectral imaging. *Adv. Mater.* **2017**, *29*, 1703510.
- (9) Willis, R.; Feuerbacher, B.; Fitton, B. Graphite conduction band states from secondary electron emission spectra. *Phys. Lett. A* **1971**, *34*, 231–233.
- (10) Hoffman, A. Fine structure in the secondary electron emission spectrum as a spectroscopic tool for carbon surface characterization. *Diamond Relat. Mater.* **1994**, *3*, 691–695.
- (11) Dapor, M. *Transport of Energetic Electrons in Solids*; Springer International Publishing: Cham, **2017**, 10.1007/978-3-319-47492-2.
- (12) Taioli, S.; Simonucci, S. Chapter Five - A Computational Perspective on Multichannel Scattering Theory with Applications to Physical and Nuclear Chemistry. *Annu. Rep. Comput. Chem.* **2015**, *11*, 191–310.
- (13) Taioli, S.; Simonucci, S.; Calliari, L.; Dapor, M. Electron spectroscopies and inelastic processes in nanoclusters and solids: Theory and experiment. *Phys. Rep.* **2010**, *493*, 237–319.
- (14) Taioli, S.; Simonucci, S.; Dapor, M. SURPRISES: when ab initio meets statistics in extended systems. *Comput. Sci. Discovery* **2009**, *2*, 015002.
- (15) Taioli, S.; Simonucci, S.; Calliari, L.; Filippi, M.; Dapor, M. Mixed ab initio quantum mechanical and Monte Carlo calculations of secondary emission from SiO₂ nanoclusters. *Phys. Rev. B: Condens. Matter Mater. Phys.* **2009**, *79*, 085432.
- (16) The Elk FP-LAPW Code. <http://elk.sourceforge.net/> (Accessed April 5, 2016).
- (17) Dapor, M. Elastic scattering calculations for electrons and positrons in solid targets. *J. Appl. Phys.* **1996**, *79*, 8406.

- (18) Dapor, M.; Masters, R. C.; Ross, I.; Lidzey, D. G.; Pearson, A.; Abril, I.; Garcia-Molina, R.; Sharp, J.; Unčovský, M.; Vystavel, T.; Mika, F.; Rodenburg, C. Secondary electron spectra of semi-crystalline polymers—A novel polymer characterisation tool? *J. Electron Spectrosc. Relat. Phenom.* **2018**, *222*, 95–105.
- (19) Ganachaud, J.; Mokrani, A. Theoretical study of the secondary electron emission of insulating targets. *Surf. Sci.* **1995**, *334*, 329.
- (20) Tanuma, S.; Powell, C.; Penn, D. Calculations of electron inelastic mean free paths. IX. Data for 41 elemental solids over the 50 eV to 30 keV range. *Surf. Interface Anal.* **2011**, *43*, 689.
- (21) Azzolini, M.; Morresi, T.; Garberoglio, G.; Calliari, L.; Pugno, N. M.; Taioli, S.; Dapor, M. Monte Carlo simulations of measured electron energy-loss spectra of diamond and graphite: Role of dielectric-response models. *Carbon* **2017**, *118*, 299.
- (22) Royal Society of Chemistry. Periodic Table: Carbon. <http://www.rsc.org/periodic-table/element/6/carbon> (Accessed March 10, 2016).
- (23) Garcia-Molina, R.; Abril, I.; Denton, D.; Heredia-Avalos, S. Allotropic effects on the energy loss of swift H⁺ and He⁺ ion beams through thin foils. *Nucl. Instrum. Methods Phys. Res., Sect. B* **2006**, *249*, 6–12.
- (24) Zhou, Y.; Fox, D. S.; Maguire, P.; O'Connell, R.; Masters, R.; Rodenburg, C.; Wu, H.; Dapor, M.; Chen, Y.; Zhang, H. Quantitative secondary electron imaging for work function extraction at atomic level and layer identification of graphene. *Sci. Rep.* **2016**, *6*, 21045.
- (25) Garcia-Molina, R.; Abril, I.; Kyriakou, I.; Emfietzoglou, D. Inelastic scattering and energy loss of swift electron beams in biologically relevant materials. *Surf. Interface Anal.* **2017**, *49*, 11–17.
- (26) Emfietzoglou, D.; Kyriakou, I.; Garcia-Molina, R.; Abril, I. Inelastic mean free path of low-energy electrons in condensed media: beyond the standard models. *Surf. Interface Anal.* **2017**, *49*, 4–10.
- (27) Emfietzoglou, D.; Kyriakou, I.; Garcia-Molina, R.; Abril, I. The effect of static many-body local-field corrections to inelastic electron scattering in condensed media. *J. Appl. Phys.* **2014**, *114*, 144907.
- (28) Jülich Supercomputing Centre. JUQUEEN: IBM Blue Gene/Q Supercomputer System at the Jülich Supercomputing Centre. *Journal of Large-Scale Research Facilities* **2015**, *1*, A1.